

See discussions, stats, and author profiles for this publication at: <https://www.researchgate.net/publication/330372032>

Adaptive Superpixel Generation for SAR Images With Linear Feature Clustering and Edge Constraint

Article in IEEE Transactions on Geoscience and Remote Sensing · January 2019

DOI: 10.1109/TGRS.2018.2888891

CITATIONS

0

READS

86

5 authors, including:



Deliang Xiang

KTH Royal Institute of Technology

42 PUBLICATIONS 266 CITATIONS

[SEE PROFILE](#)



Tao Tang

24 PUBLICATIONS 206 CITATIONS

[SEE PROFILE](#)



Sinong Quan

National University of Defense Technology

11 PUBLICATIONS 16 CITATIONS

[SEE PROFILE](#)



Yi Su

Hunan Agricultural University

78 PUBLICATIONS 825 CITATIONS

[SEE PROFILE](#)

Some of the authors of this publication are also working on these related projects:



Fine Description of Building Scattering Mechanism and the Key Techniques in Information Extraction with Polarimetric SAR [View project](#)



SAR/PolSAR Image Processing [View project](#)

Adaptive Superpixel Generation for SAR Images With Linear Feature Clustering and Edge Constraint

Deliang Xiang^{ID}, Tao Tang^{ID}, Sinong Quan^{ID}, Dongdong Guan^{ID}, and Yi Su, *Senior Member, IEEE*

Abstract—Due to the speckle noise and complex geometric distortions within SAR images, it is still a challenge to develop a stable method that can produce superpixels with both high boundary adherence and visual compactness with low computational costs at the same time. In this paper, we propose an adaptive superpixel generation approach with linear feature clustering and edge constraint for synthetic aperture radar (SAR) images, which consists of three stages. First, the local gradient ratio pattern of each pixel in SAR imagery is extracted as features, which was previously proposed by us for SAR target recognition and has been proven to be insensitive to speckle noise. Second, we propose to use the feature-ratio-based edge detector with Gauss-shaped window instead of the traditional rectangle-shaped window to obtain the edge strength map and final edges for SAR images. Finally, a modified normalized cut (Ncut)-based superpixel generation strategy is adopted using a distance metric that simultaneously measures both the feature similarity and space proximity. In this strategy, we approximate the similarity measure through a positive semidefinite kernel function rather than directly using the traditional eigen-based algorithm. Therefore, the objective functions of weighted local K-means and Ncuts can achieve the same optimum point by appropriately weighting each point in this feature space, which greatly reduces the computation cost. During the linear feature clustering, the coefficient of variation is used to automatically determine the tradeoff factor between the feature similarity and space proximity, which helps change the superpixel shape and size adaptively according to the image homogeneity. Furthermore, the edge information is also introduced to constrain the clustering for the sake of high boundary adherence. By bridging the local K-means clustering and Ncuts, as well as the benefits of edge constraint, our method not only produces superpixels with good boundary adherence but also captures the global image structure information. Experimental results with simulated and real SAR images demonstrate the effectiveness of our proposed method, which performs better than other state-of-the-art algorithms.

Index Terms—Edge constraint, linear feature clustering, normalized cuts (Ncuts), superpixel generation, synthetic aperture radar (SAR), weighted local K-means.

Manuscript received July 19, 2018; revised October 30, 2018; accepted December 16, 2018. This work was supported in part by the National Natural Science Foundation of China under Grant 41801236 and Grant 61701508 and in part by the Hunan Provincial Natural Science Foundation of China under Grant 2017JJ2304. (*Corresponding author: Tao Tang*)

D. Xiang is with the National Innovation Institute of Defense Technology, Beijing 100091, China (e-mail: xiangdeliang@gmail.com).

T. Tang, S. Quan, D. Guan, and Y. Su are with the College of Electronic Science, National University of Defense Technology, Changsha 410073, China (e-mail:tangtaonudt@gmail.com).

Color versions of one or more of the figures in this paper are available online at <http://ieeexplore.ieee.org>.

Digital Object Identifier 10.1109/TGRS.2018.2888891

I. INTRODUCTION

SYNTHETIC aperture radar (SAR) system is a promising and widely used technique for remote sensing since it is capable of providing high-resolution images of the land covers under day-or-night and all-weather conditions. With the development of SAR sensors, more and more data can be obtained. Therefore, developing automatic or semiautomatic techniques for SAR image interpretation and information mining is urgently required and widely studied [1], [2].

Superpixel generation is an increasingly popular fundamental image preprocessing approach, which plays a key role in many computer vision applications such as image segmentation, classification, target identification, change detection, and denoising [3]–[8]. The goal of superpixel generation is actually oversegmentation, which provides a concise image representation by grouping pixels with similar attributes into local, coherent regions which adhere well to image boundaries [9]. The local region, i.e., superpixel, can preserve most of the information of the grouped pixels. Therefore, the image postprocessing can be performed based on the superpixels instead of pixels, which is useful in reducing the complexity and processing time of the images [9], [10].

There have been proposed many superpixel generation algorithms including normalized cuts (Ncuts) [11], mean shift [12], Turbopixel [13], and simple linear iterative clustering (SLIC) [9], which are all originally designed for natural images. However, there are very few superpixel generation algorithms proposed for SAR images. Some studies utilized these methods directly for SAR images without considering the speckle noise [14], [15], leading to unsatisfactory results in some cases. Xiang *et al.* [5] proposed a superpixel generation approach based on the similarity between pixel intensity and location, which modified the similarity measure of SLIC to make it suitable for SAR images. Zou *et al.* [16] utilized the generalized gamma distribution to model SAR images and combined the spatial context with likelihood information to remove small isolated regions. Akyilmaz and Leloglu [17] proposed to use the Mahalanobis distance (MD) instead of the Euclidian distance and further combined it with a similarity ratio term between pixels, achieving good performance on SAR images. Song *et al.* [18], Feng *et al.* [19], and Qin *et al.* [20] adopted the Bartlett distance, symmetric revised Wishart distance, and revised Wishart distance, respectively, to replace the similarity measure in the SLIC to generate

superpixels for polarimetric SAR images. To further improve the superpixel generation accuracy of heterogeneous urban areas, Xiang *et al.* [21] proposed an adaptive superpixel generation method which utilized a homogeneity measurement to automatically control the balance between superpixel shape and compactness. Note that these methods are all designed based on the SLIC approach for the reason that this method is superior in terms of both boundary adherence and computational efficiency in comparison with the state-of-the-art superpixel approaches [9]. Nevertheless, as a local clustering-based algorithm, the relationship between SLIC and global image information is not clear. These methods may fail to correctly generate superpixels in the image area with low intensity variability. It is validated that global image information is important for human vision cognition and should be considered in image interpretation since the nonlocal clues are critical to group distant image pixels into semantically meaningful regions [11], [22]. However, considering global relationship among pixels usually significantly increases the computational complexity.

Entropy rate superpixel (ERS) generation algorithm achieves promising results on the superpixel generation benchmark by maximizing a clustering objective function [23]. Compared with the SLIC method, ERS has the potential to generate size-adaptive superpixels considering the image global properties. Wang *et al.* [3] proposed to introduce the ERS method into polarimetric SAR image superpixel generation by integrating two different distances to measure the dissimilarity between neighboring pixels. However, the irregular shape of ERS-based superpixels may become a potential drawback in the following feature extraction. The Ncuts superpixel generation algorithm [11] is widely known because it can produce superpixels with regular shape and relatively high boundary adherence. In addition, the global image properties are also well considered. Liu *et al.* [6] incorporated the revised Wishart distance and edge map of polarimetric SAR images into the Ncuts to produce superpixels. Nevertheless, the traditional eigen-based solution involved in the Ncuts has extremely high computational complexity, which decreases the superpixel generation efficiency and further limits its applicability.

It is worth pointing out most of the aforementioned SAR image superpixel generation methods redefined the similarity measure between pixels based on the image statistical distributions. However, it is generally not easy to find an accurate distribution to model the SAR image clutter, especially for the imagery with complex scenes and high resolutions [21], [24]. In addition, multiple cues involved in the similarity measure of these methods are usually balanced with a fixed tradeoff factor, which cannot change the superpixel shape and size adaptively according to the image content. Furthermore, the image structure information is not carefully considered during the superpixel generation with low computational cost, making the final superpixel map cannot well preserve the global image properties with high efficiency at the same time.

To address the above problems, we propose an adaptive superpixel generation approach with linear feature clustering

and edge (ALFCE) constraint for SAR images, which not only considers the important global image information but also runs in linear clustering with high computation efficiency. We first extract the local gradient ratio pattern (LGRP) feature for each pixel, which has been proven to be insensitive to speckle. A feature-ratio-based detector with Gauss-shaped window instead of traditional rectangle-shaped window is then proposed to obtain the edge strength map and final edges for SAR images. The Ncuts superpixel generation strategy is adopted using a distance metric that measures both the feature similarity and the space proximity. However, instead of using the traditional eigen-based optimization solution, we utilized weighted K -means clustering by approximating the similarity measure through a positive semidefinite kernel function to achieve the optimal cost. The coefficient of variation (CoV) is used to automatically determine the tradeoff factor between feature similarity and space proximity, which helps change the superpixel shape and size adaptively according to the image homogeneity. Moreover, the edge information is also introduced to constrain the clustering for preserving high boundary adherence. The proposed superpixel generating method has the following four characteristics: 1) the image structure can be well preserved due to the Ncuts strategy and edge information; 2) the method is insensitive to speckle noise in SAR; 3) it has high computational efficiency; and 4) it can change the superpixel shape and compactness adaptively according to the image content complexity.

The remaining content is organized as follows. Section II introduces the feature extraction of LGRP for SAR images, followed by the feature-based ratio edge detector with Gauss-shaped window described in Section III. Section IV gives the details of our proposed superpixel generation methodology, and Section V presents the experimental results, discussions, and in-depth comparisons with other methods. Conclusions are provided in Section VI.

II. LOCAL GRADIENT RATIO PATTERN FEATURE

In this section, we introduce the LGRP feature for SAR images, which was previously proposed by us for SAR target recognition [25]. This feature extraction approach was inspired by the idea of local binary pattern (LBP) and considered the pixel ratio measurement, which has been proven to be insensitive to multiplicative speckle noise and small or large image gradient variation in SAR images [25], [26]. Therefore, it has a potential ability to benefit the superpixel generation. Moreover, the implementation of LGRP is simple and its computational complexity is low, ensuring the high efficiency of our proposed approach.

The LBP is calculated based on the Euclidean distance between the neighborhood pixel and the center pixel and has a good performance in the feature extraction and description for image textures [27]. LBP has been extensively used in the texture description and image classification due to its simple implementation and rotation invariance.

A sliding 3×3 window is used to calculate the LBP algorithm, which can describe the local structure of an image.

The calculation of LBP can be expressed as [27]

$$\text{LBP}_{P,R} = \sum_{p=0}^{P-1} s(g_p - g_c)2^p, \quad s(x) = \begin{cases} 1, & x \geq 0 \\ 0, & x < 0 \end{cases} \quad (1)$$

where g_c and g_p are the gray values of center and neighborhood pixels, respectively. R is the neighborhood radius of center pixel, and P is the number of neighborhood pixels.

Although LBP is suitable for the image texture description, it does not perform well on SAR images due to the multiplicative speckle. In the implementation of LGRP, the gradient value of each pixel in the neighborhood is calculated as the gray value difference between itself and the center pixel. Then, its gradient ratio pattern can be obtained as depicted in (2), namely, the ratio of its gradient value and initial gray value. This is a simplified version of the pixel ratio measurement, which has been proven to be insensitive to the multiplicative speckle noise [5], [25], [28]. Afterward, the gradient ratio pattern of the center pixel is regarded as the average pattern values of all the neighborhood pixels, as shown in (3). After that, similar to LBP, the LGRP operator is calculated at the center pixel by evaluating the binary differences of the gradient ratio pattern values with the neighborhood pixels, as depicted in (4)

$$G_{\text{ratio}}(g_p) = \frac{|g_p - g_c|}{g_p} \quad (2)$$

$$\overline{G_{\text{ratio}}(g_c)} = \frac{1}{P} \sum_{p=1}^P G_{\text{ratio}}(g_p) \quad (3)$$

$$\text{LGRP}_{P,R}(g_c) = \sum_{p=0}^{P-1} s(G_{\text{ratio}}(g_p) - \overline{G_{\text{ratio}}(g_c)})2^p \quad (4)$$

where $G_{\text{ratio}}(g_p)$ and $\overline{G_{\text{ratio}}(g_c)}$ are the gradient ratio patterns of the neighborhood pixel g_p and the center pixel g_c , respectively. $s(\cdot)$ is a sign function, which is the same as that depicted in (1).

It is worth pointing out that the local image intensities of neighbor pixels and the gradient information of SAR images are both taken into account in the calculation of LGRP, as depicted in (2). Due to the reason that the pixel ratio measurement is integrated into the LGRP definition, this feature is insensitive to the multiplicative speckle noise. Another advantage is that it is well adaptive to SAR images with various gradient variations, which are common phenomenon in SAR images with complex scenes. Therefore, this feature has the abilities which can improve the superpixel generation performance of SAR images. Further details about LGRP feature extraction can be found in [25].

III. FEATURE-RATIO-BASED EDGE DETECTOR

Since image edge contains most of the useful structural information and is beneficial to distinguish different image regions, the edge information is important for superpixel generation and segmentation [29], [30]. Until now, there have been proposed some edge detectors for SAR images; among them, techniques based on the ratio between neighboring pixels are popular, which are known as the ratio-based edge

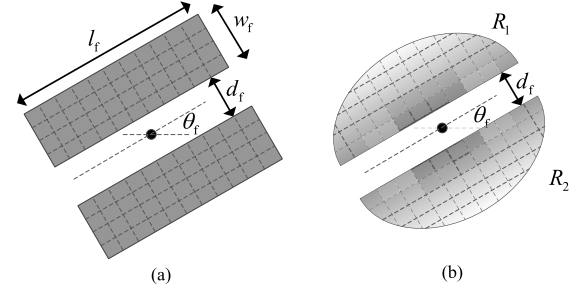


Fig. 1. Filter configuration at orientation $\pi/4$. (a) Rectangle-shaped filter. (b) Gauss-shaped filter.

detectors [31], [32]. A rectangle-shaped window centered at the current pixel is divided into two parallel sub windows on the opposite sides. The ratio of the amplitude means within two subwindows is a test statistic for SAR image edge detection. Note that the rectangle-shaped window usually has a remarkable sidelobe, and also due to the multiplicative speckle within SAR images, these intensity-ratio-based edge detectors are apt to incur many false-edge pixels in the scenes with low gradient variations. To resolve this problem, we introduce to use the LGRP feature and the Gauss-shaped window instead of the traditional rectangle-shaped window to achieve SAR image edge detection, which can improve the localization precision and keep the false positive rate low.

A. Window Configuration

The traditional rectangle-shaped edge detectors use a set of rectangular windows with different orientations on each pixel to calculate the edge strength map [31]–[36]. This window is split into a pair of parallel sub windows, as shown in Fig. 1(a). The window configurations consist of four parameters, namely, the window width w_f , the window length l_f , the spacing d_f between two subwindows, and the angular increment θ_f between two orientations. The ratio distance of amplitude means in two subwindows at different orientations is collected as a measure of the probability of an edge pixel. Finally, the maximum distance from different sets of windows is utilized to construct a ratio-based edge strength map. Note that the local mean functions using a rectangle-shaped window contain some unwanted high-frequency components [32], which may yield false local maxima and further result in false-edge pixels.

Different from the rectangle-shaped window, in this paper, we use a Gauss-shaped window to overcome the above limitations, as depicted in Fig. 1(b). The spacing d_f and angular increment θ_f in Fig. 1(b) have the exact same definitions as those in Fig. 1(a). The horizontal Gauss-shaped window function is defined as

$$\text{GW}(x, y) = \frac{1}{\sqrt{2\pi}\sigma_x\sqrt{2\pi}\sigma_y} \exp\left(-\left(\frac{x^2}{2\sigma_x^2} + \frac{y^2}{2\sigma_y^2}\right)\right) \quad (5)$$

where $\text{GW}(x, y)$ is the Gauss weight of pixel (x, y) , which will be used for the average of LGRP feature of the center pixel on both sides of the split window. The window length and width are controlled by σ_x and σ_y , respectively. It is

worth pointing out that different from the same weight in the rectangle-shaped window, pixels have larger Gauss weights if they are close to the center pixel, as depicted in (5) and Fig. 1(b). This is consistent with the fact that when checking whether the center pixel is an edge or not, pixels near the center pixel usually have more useful information than other pixels. Therefore, it is beneficial for the edge detection since more accurate local means can be obtained using this window. The Gauss-shaped window with orientation angle θ_f can be obtained by rotating (5) like

$$\text{GW}^{\theta_f}(x, y) = \text{GW}(x \cos \theta_f - y \sin \theta_f, x \sin \theta_f + y \cos \theta_f) \quad (6)$$

B. Edge Detection Approach

Instead of using the local means of SAR amplitude values for edge detection, in this paper, we calculate the local means of LGRP feature values with the Gauss-shaped window. The main advantage is that LGRP is insensitive to the multiplicative speckle, and it has the capacity to describe SAR images with high or low gradient variation. Therefore, the false-edge pixels in the scenes with different gradient variations can be prevented.

The local means of LGRP features for pixel (x, y) at orientation angle θ_f are calculated by convolving the Gauss-shaped window function with the feature values as

$$\begin{aligned} \text{LGRP}_{\text{mean}}(x, y|\theta_f) \\ = \sum_{(x', y')} \text{GW}^{\theta_f}(x', y') \text{LGRP}(x - x', y - y') \end{aligned} \quad (7)$$

Note that the orientation angle θ_f is discretized into $\theta_f = 0, \pi/N_f, \dots, \pi(N_f - 1)/N_f$, where N_f is the number of window orientations. After that, the similarity of local means of LGRP features on both sides of the central pixel (x, y) can be calculated by a ratio distance as

$$R(x, y) = \min_{f=0,1,\dots,N_f-1} \left\{ \min \left\{ \frac{\text{LGRP}_{\text{mean}}^U(x, y|\theta_f)}{\text{LGRP}_{\text{mean}}^L(x, y|\theta_f)}, \frac{\text{LGRP}_{\text{mean}}^L(x, y|\theta_f)}{\text{LGRP}_{\text{mean}}^U(x, y|\theta_f)} \right\} \right\} \quad (8)$$

where f is the indicator of current window orientation and superscripts U and L denote the upper and lower subwindow, respectively, on two sides of the center pixel (x, y) . Then the edge strength map (ESM) and the edge direction map (EDM) are obtained as follows:

$$\text{ESM} = 1 - R(x, y) \quad (9)$$

$$\text{EDM} = \arg \min_{\theta_f} R(x, y) + \pi/2 \quad (10)$$

where EDM gives the direction along which the amplitude variation at pixel (x, y) is maximal. Inherited from the framework of other ratio-based edge detectors [31], [32], this improved approach is given as follows.

Input: SAR amplitude image

Output: ESM, EDM, and edge map

- 1) For each pixel of a given SAR image, calculate its ESM and EDM with (9) and (10), respectively.

- 2) Perform the nonmaximum suppression [37] on ESM to find the maximum values. All the maxima of ESM construct the set of candidate edge pixels Ω_E .
- 3) Define two thresholds Th_H and $\text{Th}_L (< \text{Th}_H)$. For each candidate pixel in Ω_E , if its ESM is bigger than Th_H , it can be declared as a strong edge. If its ESM is between Th_H and Th_L , it is decided as edge pixels only when there is a strong edge in its four or eight neighborhoods. Otherwise, it is removed from Ω_E . Finally, a binary edge map is obtained by setting the edge pixel to one.

C. Computational Complexity Analysis of Edge Detection

If ignoring the LGRP feature extraction, the computational complexity of this improved edge detection is the same as those of other ratio-based edge detectors [31], [32]. For dealing with an SAR image with size $M \times N$, the computational complexity is $O(N_f MN \sigma_L \sigma_W)$, where σ_L and σ_W denote the length and width of the Gauss-shaped window, respectively. It can be seen that the computational complexity is dramatically increased with the size of the Gauss-shaped window, the number of the window orientations and the size of the SAR image. The fast Fourier transform can be used to reduce the computation complexity from $O(N_f MN \sigma_L \sigma_W)$ to $O(5N_f MN(\log_2 M + \log_2 N))$.

IV. PROPOSED SUPERPIXEL GENERATION METHODOLOGY

In this section, the proposed adaptive superpixel generation algorithm with linear feature clustering and edge constraint (ALFCE) is presented in detail. Inspired by [10] and [38], through bridging the weighted local K -means feature clustering and the Ncuts method, our ALFCE has the ability not only to produce superpixels for SAR images with good boundary adherence but also can capture the local and global image properties. More importantly, the computation of ALFCE is highly efficient since the weighted local K -means feature clustering is utilized to replace the serious complex eigen-based strategy in the original Ncuts method for minimizing its objective function. Furthermore, the edge information is also considered in the weighted linear feature clustering, which is beneficial to preserve the image structure and further produce semantically meaningful superpixels. We first give the Ncuts optimization with weighted local K -means feature clustering, followed by the similarity definition for the superpixel generation. Finally, the detailed implementation of ALFCE is presented.

A. Normalized Cuts Optimization With Weighted Local K -means

To facilitate the optimization, we revisit the definitions of weighted local K -means feature clustering and the Ncuts approach and try to investigate the relationship between the objective functions involved within these two methods. In the weighted local K -means clustering, let K be the total number of clusters and m_k be the center of k th cluster $\omega(k)$, where $k = 1, 2, \dots, K$. The weighted local K -means feature clustering aims to partition N original observations into K clusters

through mapping the observations into new feature space with different weights. The partition is optimal when obtaining minimal objective function, which measures the weighted within-cluster sum of squares. We use a function Ψ to map the original data points to a high dimensional feature space to improve the data discrimination ability. Each feature point p in the high dimensional feature space Ω is assigned with a weight $w(p)$. Then the objective function of weighted local K -means clustering can be defined as [38]

$$\Phi_{K\text{-means}} = \sum_{k=1}^K \sum_{p \in \omega(k)} w(p) \|\Psi(p) - m_k\|^2 \quad (11)$$

where the center m_k of k th cluster $\omega(k)$ is calculated as

$$m_k = \frac{\sum_{q \in \omega(k)} w(q) \Psi(q)}{\sum_{q \in \omega(k)} w(q)}. \quad (12)$$

Note that the objective function $\Phi_{K\text{-means}}$ can be minimized with an iterative strategy until the termination criterion can be achieved [38].

In the Ncuts algorithm, the set of points in an arbitrary feature space is represented as a weighted undirected graph $G = (V, E, W)$. Each data point p in the feature space can be represented as a node in this graph, where V denotes the set of all nodes, E represents the set of edges between two arbitrary pair of nodes, and W stands for the similarity function, which denotes the weight on each edge. In local regions grouping, the set of nodes should be partitioned into disjoint sets, where by some measures the similarity among the nodes in a set is high and, across different sets is low. Shi and Malik [11] proposed to compute the cut cost as a fraction of the total edge connections to all the nodes in the graph and then solved the solution through maximizing the objective function as

$$\Phi_{\text{Ncuts}} = \frac{1}{K} \sum_{k=1}^K \frac{\sum_{p \in \omega(k)} \sum_{q \in \omega(k)} W(p, q)}{\sum_{p \in \omega(k)} \sum_{q \in V} W(p, q)} \quad (13)$$

where $W(p, q)$ denotes the similarity measure between two points p and q . This objective function can be solved with the eigenvalue decomposition of the large affinity matrix [11]. Nevertheless, this solution is quite computationally complex, especially when the number of superpixels increases, making the efficiency of the Ncuts algorithm not high. In addition, the local image properties are not considered in this method since the solution is based on the decomposition of whole image affinity matrix.

Dhillon *et al.* [38] presented the relationship between weighted local K -means clustering and Ncuts by rewriting the optimization of objective functions $\Phi_{K\text{-means}}$ and Φ_{Ncuts} . A kernel matrix which maps data points into higher dimensional feature space is introduced and the optimization of $\Phi_{K\text{-means}}$ and Φ_{Ncuts} can be regarded as the same matrix trace maximization problem. After that, Chen *et al.* [10] and Li and Chen [39] further revealed the relationship between the two objective functions more clearly and tried to define a positive definite kernel matrix. In this paper, we extend the results in [10] and [38] in a more explicit way for SAR images and give the theory foundation of ALFCE superpixel generation.

The objective functions of the weighted K -means and Ncuts can be optimized in a mathematically equivalent way when the following two conditions are satisfied [38]:

$$\forall p, q \in V, \quad w(p)\Psi(p) \cdot w(q)\Psi(q) = W(p, q) \quad (14)$$

$$\forall p \in V, \quad w(p) = \sum_{q \in V} W(p, q) \quad (15)$$

where the operator \cdot denotes the inner product between two feature vectors. The first condition denotes that the inner product of two weighted feature vectors in the high dimensional feature space equals the similarity between the two corresponding data points in the original space. The second condition indicates that the weight of each point in the weighted local K -means clustering equals the total weight of edges in the Ncuts algorithm which connect the corresponding node to all the other nodes in the graph. With (11) and (12), the objective function of weighted local K -means clustering $\Phi_{K\text{-means}}$ can be expanded and rewritten as in (16), shown at the top of the next page.

In (16), the first item is a constant, which is independent of the weighted K -means clustering result. Given the conditions depicted in (14) and (15), we further rewrite (16) as (17), where it can be easily found that minimizing the objective function of the weighted K -means clustering is equivalent to maximizing that of the Ncuts algorithm

$$\begin{aligned} \Phi_{K\text{-means}} &= C - \sum_{k=1}^K \frac{\sum_{p \in \omega(k)} \sum_{q \in \omega(k)} w(p) \Psi(p) \times w(q) \Psi(q)}{\sum_{p \in \omega(k)} w(p)} \\ &= C - \sum_{k=1}^K \frac{\sum_{p \in \omega(k)} \sum_{q \in \omega(k)} W(p, q)}{\sum_{p \in \omega(k)} \sum_{q \in V} W(p, q)} \\ &= C - K \times \Phi_{\text{Ncuts}}. \end{aligned} \quad (17)$$

Among the two conditions, (15) can be easily achieved by regarding the total edge weights in Ncuts as the corresponding point weight in weighted K -means clustering. Therefore, it can be concluded that by carefully choosing a mapping function Ψ , which constructs the high dimensional feature space to make the weighted inner products in the feature space to be equal to the similarity measurement in the input space, the objective function optimizations of the weighted local K -means clustering and the normalized cut are mathematically equivalent. In the first condition (14), since the left-hand side is the inner product of two vectors in the high dimensional feature space, (14) can be considered as the definition of a symmetric kernel function. Therefore, the similarity measure W must satisfy the positivity condition and also should be separable to achieve the mapping function Ψ with an explicit expression.

B. Similarity Measure Definition

It can be indicated that one core of our proposed ALFCE approach is to find a suitable similarity measure $W(p, q)$ to fulfill the first condition in (14). Consequently, this subsection presents the similarity measure definition for SAR image superpixel generation, which considers the local feature and spatial information at the same time. Moreover, the CoV is

$$\begin{aligned}
\Phi_{\text{K-means}} &= \sum_{k=1}^K \sum_{p \in \omega(k)} w(p) \left\| \Psi(p) - \frac{\sum_{q \in \omega(k)} w(q) \Psi(q)}{\sum_{q \in \omega(k)} w(q)} \right\|^2 \\
&= \sum_{k=1}^K \sum_{p \in \omega(k)} w(p) \|\Psi(p)\|^2 - \sum_{k=1}^K \left(2 \sum_{p \in \omega(k)} w(p) \Psi(p) \times \frac{\sum_{q \in \omega(k)} w(q) \Psi(q)}{\sum_{q \in \omega(k)} w(q)} \right) \\
&\quad + \sum_{k=1}^K \left(\sum_{p \in \omega(k)} w(p) \left\| \frac{\sum_{q \in \omega(k)} w(q) \Psi(q)}{\sum_{q \in \omega(k)} w(q)} \right\|^2 \right) \\
&= \sum_{k=1}^K \sum_{p \in \omega(k)} w(p) \|\Psi(p)\|^2 - \sum_{k=1}^K \left(2 \frac{\left\| \sum_{p \in \omega(k)} w(p) \Psi(p) \right\|^2}{\sum_{p \in \omega(k)} w(p)} \right) + \sum_{k=1}^K \left(\frac{\left\| \sum_{p \in \omega(k)} w(p) \Psi(p) \right\|^2}{\sum_{p \in \omega(k)} w(p)} \right) \\
&= \sum_{k=1}^K \sum_{p \in \omega(k)} w(p) \|\Psi(p)\|^2 - \sum_{k=1}^K \frac{\left\| \sum_{p \in \omega(k)} w(p) \Psi(p) \right\|^2}{\sum_{p \in \omega(k)} w(p)} \\
&= \sum_{k=1}^K \sum_{p \in \omega(k)} w(p) \|\Psi(p)\|^2 - \sum_{k=1}^K \frac{\sum_{p \in \omega(k)} \sum_{q \in \omega(k)} w(p) \Psi(p) \times w(q) \Psi(q)}{\sum_{p \in \omega(k)} w(p)}. \tag{16}
\end{aligned}$$

used to automatically determine the tradeoff factor between feature similarity and space proximity, which is beneficial to change the superpixel shape and size adaptively according to the image homogeneity.

For each pixel p in an SAR amplitude image, we use a four dimensional vector $p = (l_{4p}, l_{8p}, x_p, y_p)$ to represent it, where l_{4p} and l_{8p} denote the LGRP features of pixel p with four- and eight-neighborhoods, respectively. x_p and y_p are the pixel coordinates in the SAR image plane. It is worth pointing out that compared with the LGRP feature with a single neighborhood, LGRP features with different neighborhoods can obtain more useful information about the gradient variation in SAR images [25], which is useful for superpixel generation. The range of each component in the vector should be linearly normalized to $[0, 1]$ for simplicity. Considering that the LGRP feature is insensitive to multiplicative speckle noise and different image gradient variations in SAR images, we can believe that the Euclidean distance has the potential ability to be used as the similarity measure between two pixels for the reason that its implementation is simple and efficient. Given two pixels $p = (l_{4p}, l_{8p}, x_p, y_p)$ and $q = (l_{4q}, l_{8q}, x_q, y_q)$, a similarity measurement based on the Euclidean distance between them is defined as

$$\hat{W}(p, q) = \hat{W}_f(p, q) + \beta_{\text{adp}} \cdot \hat{W}_s(p, q) \tag{18}$$

where $\hat{W}_f(p, q)$ and $\hat{W}_s(p, q)$ are the feature similarity and space proximity, respectively, and are defined as

$$\hat{W}_f(p, q) = [1 - (l_{4p} - l_{4q})^2 + 1 - (l_{8p} - l_{8q})^2] \tag{19}$$

$$\hat{W}_s(p, q) = [1 - (x_p - x_q)^2 + 1 - (y_p - y_q)^2]. \tag{20}$$

Parameter β_{adp} in (18) is used as a weighting factor to control the relative significance of feature and spatial information, which is usually chosen to be a constant in most of the superpixel generation methods [5], [9], [10], [16], [20].

This parameter is generally set manually by trial and error, which may lead to over- or under-superpixel segmentation in some SAR images with spatially complicated scenes. Therefore, developing an adaptive parameter according to the image homogeneity helps change the superpixel shape and size adaptively. In this paper, we utilize the CoV of the image scene, which is derived from the ratio of standard deviation to mean value for each pixel. Parameter β_{adp} can be defined as

$$\beta_{\text{adp}} = 1 - \frac{1}{2} [\text{CoV}(x_p, y_p) + \text{CoV}(x_q, y_q)] \tag{21}$$

where it can be seen that this adaptive factor considers the CoV of two compared pixels and has the range $[0, 1]$. From (18) and (21), it can be found that for homogeneous areas without too much edge information, β_{adp} is high, then the spatial proximity outweighs the feature similarity measure, leading to compact superpixels. Nevertheless, for heterogeneous areas, β_{adp} is low and can suppress the spatial proximity. Consequently, the superpixels are generated mainly with the LGRP feature information, which can well adhere to image boundaries.

Even though $\hat{W}(p, q)$ is an adaptive pixel similarity measurement and has a very clear physical meaning, it cannot be directly used in the proposed ALFCE method for the reason that the positivity condition required by (14) is not satisfied with the Euclidean distance [40]. To resolve this problem, inspired by [10] and [38], we try to find a proper approximation of $\hat{W}(p, q)$. The function $g(t) = 1 - t^2$ where $t = x - y$ ($t \in [-1, 1]$) is introduced into (19) and (20), then $\hat{W}(p, q)$ can be rewritten as

$$\begin{aligned}
\hat{W}(p, q) &= [g(l_{4p} - l_{4q}) + g(l_{8p} - l_{8q})] \\
&\quad + \beta_{\text{adp}} \cdot [g(x_p - x_q) + g(y_p - y_q)]. \tag{22}
\end{aligned}$$

Note that $g(t) = 1 - t^2$ can be represented as a uniformly convergent Fourier series as

$$g(t) = \sum_{m=0}^{\infty} \frac{32(-1)^m}{[(2m+1)\pi]^3} \cos\left(\frac{(2m+1)\pi t}{2}\right), \quad t \in [-1, 1]. \quad (23)$$

Since the coefficients of this series converges to 0 very quickly, $g(t)$ can be approximated using the first term as

$$g(t) \approx \frac{32}{\pi} \cos \frac{\pi t}{2}, \quad t \in [-1, 1] \quad (24)$$

where $\cos(\pi t/2)$ satisfies the positivity condition, leading to the positivity of $\hat{W}(p, q)$. By simply omitting the constant $32/\pi$, the similarity measure based on Euclidean distance $\hat{W}(p, q)$ can be further approximated as

$$\begin{aligned} W(p, q) = & \left[\cos \frac{\pi}{2} (l_{4p} - l_{4q}) + \cos \frac{\pi}{2} (l_{8p} - l_{8q}) \right] \\ & + \beta_{\text{adp}} \times \left[\cos \frac{\pi}{2} (x_p - x_q) + \cos \frac{\pi}{2} (y_p - y_q) \right]. \end{aligned} \quad (25)$$

Due to $\cos(x - y) = [\cos(x), \sin(x)] \times [\cos(y), \sin(y)]$, we can rewrite $W(p, q)$ as the inner product form shown in (14), in which the mapping function is defined as

$$\begin{aligned} \Psi(p) = \frac{1}{w(p)} \left(\cos \frac{\pi}{2} l_{4p}, \sin \frac{\pi}{2} l_{4p}, \cos \frac{\pi}{2} l_{8p}, \sin \frac{\pi}{2} l_{8p}, \right. \\ \left. \beta_{\text{adp}} \cos \frac{\pi}{2} x_p, \beta_{\text{adp}} \sin \frac{\pi}{2} x_p, \right. \\ \left. \beta_{\text{adp}} \cos \frac{\pi}{2} y_p, \beta_{\text{adp}} \sin \frac{\pi}{2} y_p \right) \end{aligned} \quad (26)$$

where $w(p)$ can be obtained with (15). It can be seen that with the definition of this mapping function and an eight-dimensional feature space, the objection function optimizations of the weighted local K -means clustering and the Ncuts are approximately equivalent. Therefore, we can optimize the objective function of Ncuts by using the weighted local K -means clustering in the eight-dimensional feature space instead of the traditional eigenvalue decomposition, which can greatly reduce the computation cost. Moreover, the global and local image properties can be both considered with the combination of these two strategies. Another advantage of the similarity measure is that it does not need the prior information about the clutter statistical distribution, which is quite difficult to be determined in SAR images with complex scenes.

C. Implementation of the Proposed Algorithm

Here, we give the detailed implementation of our proposed ALFCE superpixel generation algorithm step by step. Since the approach is iterated with the weighted local K -means clustering, the implementation procedure is similar to that of SLIC [9] except the steps before linear feature iterative clustering. The algorithm is summarized as follows.

Input: SAR amplitude image

- 1) LGRP feature calculation for each pixel using (4).
- 2) ESM, EDM, and edge map calculation.

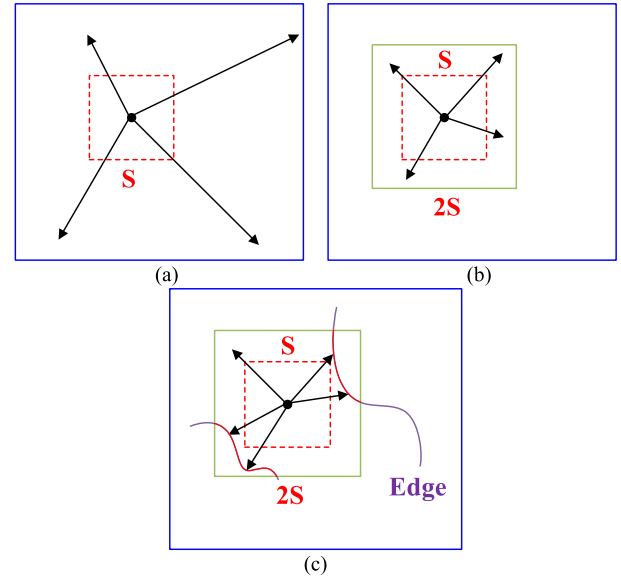


Fig. 2. Search regions for superpixel generation. (a) Weighted K -means searches the entire image. (b) SLIC searches the limited region. (c) ALFCE searches the limited region with edge constraint.

- 3) Map each point $p = (l_{4p}, l_{8p}, x_p, y_p)$ to a eight dimensional vector $\Psi(p)$.
- 4) Initialize K_s seeds over the image uniformly at regular grid steps S .
- 5) Move each seed to its lowest gradient neighbor with ESM information.
- 6) Local iterative clustering with a limited search region.
- 7) Postprocessing to eliminate the disjointed pixels as [9].

Output: superpixel map.

It should be pointed out that during the superpixel generation, the desired number of superpixels K_s is the only input. K_s seed pixels are then sampled uniformly over the whole image at regular grid steps $S = (M \times N / K_s)^{1/2}$, where $M \times N$ is the number of image pixels. Then these seeds are slightly moved to avoid the noisy and edge pixels in a 3×3 neighborhood. After that, they are used as the search centers and their feature vectors are used as the initial means. Each pixel within the search region is then assigned to the cluster of which the weighted mean is closest to the pixel's feature vector. Unlike the traditional weighted K -means and SLIC, ALFCE defines a new limited search region considering the edge constraint, as shown in Fig. 2. This search region can maintain the edge information and is also helpful to accelerate the convergence. After pixel assignment, the weighted mean and search center of each cluster should be updated. Pixels assigned to the same cluster form a superpixel after convergence of the whole procedure.

D. Computational Efficiency Analysis of ALFCE

Let the number of SAR image pixels is $M \times N$, then the complexity of LGRP feature calculation is $O(M \times N)$. As stated in Section III-C, the complexity of ESM, EDM, and edge map calculation is $O(5N_f MN(\log_2 M + \log_2 N))$. For the feature mapping, the complexity is $O(M \times N)$. During the linear iteration, it requires $O(\kappa \times M \times N)$ operations,

where κ is the number of iterations. It still needs $O(\mu z)$ operations during the postprocessing, in which z denotes the number of small isolated superpixels to be merged and μ is the number of their adjacent superpixels. Therefore, apart from the feature calculation and edge detection, the complexity of ALFCE is $O(\kappa \times M \times N + \mu z)$.

V. EXPERIMENTAL RESULTS AND ANALYSIS

In this section, we conduct experiments on both simulated and real SAR images to verify the proposed superpixel generation approach. The simulated SAR images are contaminated by multiplicative speckle with different number of looks, which are used to demonstrate the speckle robustness of our method. The real SAR images are collected by airborne and spaceborne sensors with different image resolutions, which contain mountains, urban buildings, small man-made targets airports, and other land covers. Therefore, the proposed method can be tested on different SAR scenes. First of all, we discuss the parameter settings and the performance of our proposed edge detection procedure. The existing edge detectors with exponentially weighted averages (ROEWA) [31] and Gaussian-gamma-shaped (GGS) biwindows [32] are adopted for comparison. Then, we give the superpixel generation results and comparisons of different methods using simulated and real SAR images, respectively. Three superpixel generation methods proposed for SAR images, which are the method based on pixel intensity and location similarity (PILS) [5], the likelihood-based SLIC algorithm with generalized gamma distribution (SLIC-GGD) [16] and the method based on adaptive MD measure (SLIC-MD) [17] are adopted for comparison. Finally, the computational complexity and time consumption of different methods are analyzed and compared.

A. Description of the Parameter Settings

In our proposed and several compared methods, there are some parameters need to be set before presenting the results. In the window configuration of ROEWA and GGS edge detection methods, parameters d_f, θ_f are set to 1 and $\pi/8$, respectively. The window length l_f and the width w_f are set to 11 and 5, respectively. This parameter setting works fine for various image scenes according to [31] and [32]. In order to make sure that the window areas of different edge detection methods approximate the same, in our method, the window parameters σ_x and σ_y are set to 6.4 and 3.1, respectively and d_f, θ_f are also set to 1 and $\pi/8$. The two thresholds Th_H and Th_L are set to 0.25 and 0.68, respectively, in three edge detection methods to obtain the final edges from the ESM. Regarding the number of superpixels K_s in four superpixel generation methods, there will be a detailed discussion in the following experiments. The tradeoff factor of the similarity measure in PILS, SLIC-GGD, and SLIC-MD methods are set according to [5], [16], and [17] and also the test images, which should be the optimal choices based the superpixel generation quality.

B. Performance of the Proposed Edge Detection Approach

This section gives the edge detection results of two simulated and three real SAR images with our proposed approach,

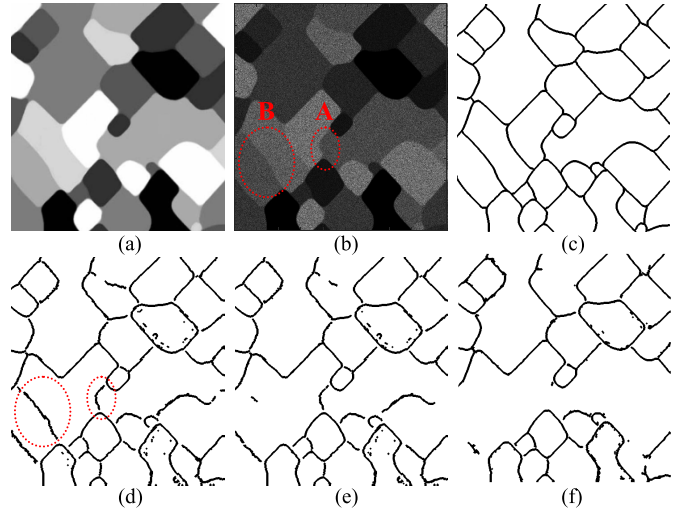


Fig. 3. Simulated SAR image with carton texture and the edge detection results. (a) Carton texture image. (b) Four-look simulated SAR image. (c) Ground truth edge image. (d)–(f) Edge maps obtained by the proposed GGS and ROEWA detectors.

as well as two compared methods, i.e., ROEWA and GGS. The simulated SAR images are generated by adding the multiplicative speckle with Gamma distribution to noise-free images with different textures. The equivalent number of looks of the speckle is set to four in the following presented results.

Fig. 3 gives the edge detection maps of simulated SAR image with carton texture using different algorithms. Fig. 3(a) shows the carton texture image, and Fig. 3(b) shows the corresponding simulated SAR image with four-look Gamma speckle. Fig. 3(c) gives the ground truth edge map. The edge detection results of our proposed GGS and ROEWA detectors are presented in Fig. 3(d)–(f), respectively. It can be seen that all the three methods can easily detect the edges between regions with obviously different texture intensities. However, for the regions with similar texture intensity, the detection performance is different. For instance, edge A in Fig. 3(b) can be detected by the proposed and GGS detectors but is omitted by the ROEWA detector. For edge B, since the two regions have quite similar texture intensity, GGS and ROEWA detectors fail to detect the edge. Nevertheless, the proposed approach can obtain this edge thanks to the contribution of LGRP feature, which has the ability in describing the image gradient variation.

Fig. 4 gives the edge detection results of simulated SAR image with shape texture using different methods. Similar to Fig. 3, it can be observed that all the three methods can detect the main edges; however, the edges of area A and B in Fig. 4(b) can only be detected with our proposed and GGS detectors. This is attributed to the nonrectangle shaped windows. Compared Fig. 4(d) with Fig. 4(e), we can find that the proposed edge detector can get better edges with fewer false edge pixels, indicating that the LGRP feature is well insensitive to the speckle and adaptive to the image gradient variation.

To quantitatively evaluate the edge detection performance of three methods, we choose the precision-recall curves using different simulated SAR images, as shown in Fig. 5.

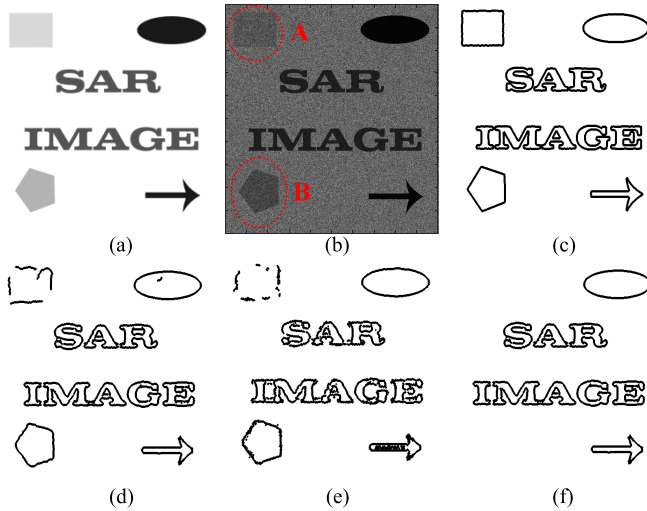


Fig. 4. Simulated SAR image with shape texture and the edge detection results. (a) Shape texture image. (b) Four-look simulated SAR image. (c) Ground truth edge image. (d)–(f) Edge maps obtained by the proposed GGS and ROEWA detectors.

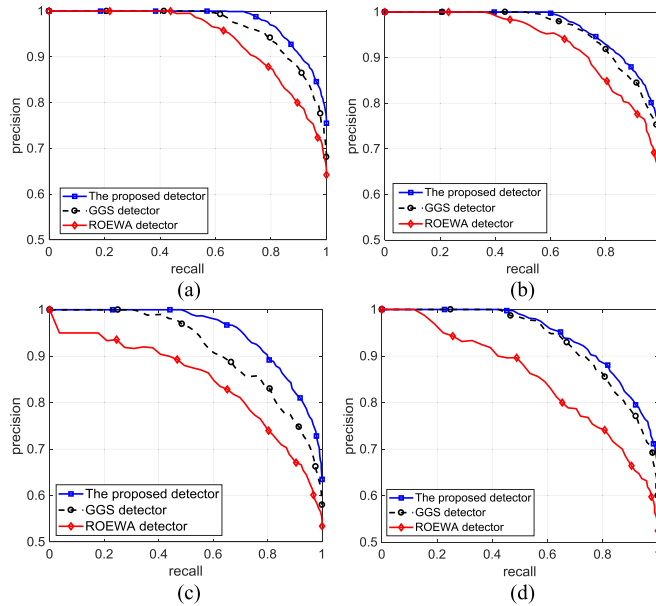


Fig. 5. Precision-recall curves of different edge detectors using (a) four-look carton texture simulated SAR image, (b) four-look shape texture simulated SAR image, (c) two-look carton texture simulated SAR image, and (d) two-look shape texture simulated SAR image.

Fig. 5(a) and (b) shows the results using four-look carton texture and shape texture simulated SAR image, respectively. It can be found that the performance of our proposed and GGS detectors is similar, whereas the results of ROEWA detector is not so good. Our method can obtain the best result among three methods due to the advantages of LGRP feature, which is insensitive to the speckle and also adaptive to the image gradient variation. To further demonstrate the speckle robustness of three edge detectors, we simulate the texture SAR images with two-look Gamma speckle and give the precision-recall curves of the edge map, as shown in Fig. 5(c) and (d). In comparison with Fig. 5(a) and (b), we can observe that the performance of ROEWA detector

TABLE I
PRECISION-RECALL VALUES OF DIFFERENT METHODS
FOR THE THREE SAR DATA SETS

Method	ESAR L band		GF-3 C band		TerraSAR X band	
	Precision	Recall	Precision	Recall	Precision	Recall
Proposed detector	0.86	0.88	0.84	0.86	0.83	0.81
GGS detector	0.81	0.78	0.79	0.80	0.78	0.76
ROEWA detector	0.75	0.71	0.59	0.63	0.73	0.71

decreases dramatically; however, our proposed and the GGS detectors can approximately maintain the detection results, indicating that these two methods are insensitive to the speckle to some extent. Furthermore, it also can be found that our proposed detector still outperforms other two methods.

Fig. 6 gives the edge detection maps of different methods for three real SAR data sets, which are airborne ESAR L band, spaceborne Chinese Gaofen 3 (GF-3) C band and TerraSAR X-band SAR images. Fig. 7 gives the ground truth edge maps of three data sets, which are drew manually according to the Google Earth maps. The first row of Fig. 6 gives the edge results of airborne ESAR L band data, where we can see that this image mainly contains urban buildings, roads, and small man-made targets, as well as some forests and farms. It can be seen from Fig. 6(b)–(d) that our proposed detector not only can obtain the obvious edges between the areas with strong and weak backscattering but also can get the weak and tiny edges accurately, as shown in the area marked with red dash circle. The result is quite similar to the ground truth edges. The middle row of Fig. 6 denotes the results of spaceborne GF-3 C band data, which image the mountain areas. It can be seen that there are some layover and shadow areas due to the side-looking SAR imaging characteristic, which result in some edges and geometric distortions. Our proposed detector can obtain most of the edges, whereas other two methods perform not so well. The bottom row of Fig. 6 shows the results of spaceborne TerraSAR X-band data, which cover an airport area. It can be observed that the edges within this image are not obvious due to the similar backscattering. However, our proposed detector can obtain most of the edges accurately; furthermore, the tiny edges of some small man-made targets also can be captured, as shown in the area marked with a red dash rectangle. The GGS detector can get similar edge maps with our method; nevertheless, the edges between runways and grass lands are not well detected, as denoted in the area with red dash circle in Fig. 6(k). The reason is that our method considers the LGRP feature, which shows superiority on the detection of image gradient variation. In comparison with our method and the GGS detector, the ROEWA detector performs not so well, indicating that it is not suitable for the SAR image with complex scenes and weak edges.

Table I depicts the precision-recall values of different methods for the three real SAR data sets, where each value in the table is calculated using the detected edges and corresponding ground truth edges, as depicted in Fig. 7. The fact that the precision and recall both have high values indicates that the edge detection result is satisfactory. We can observe from

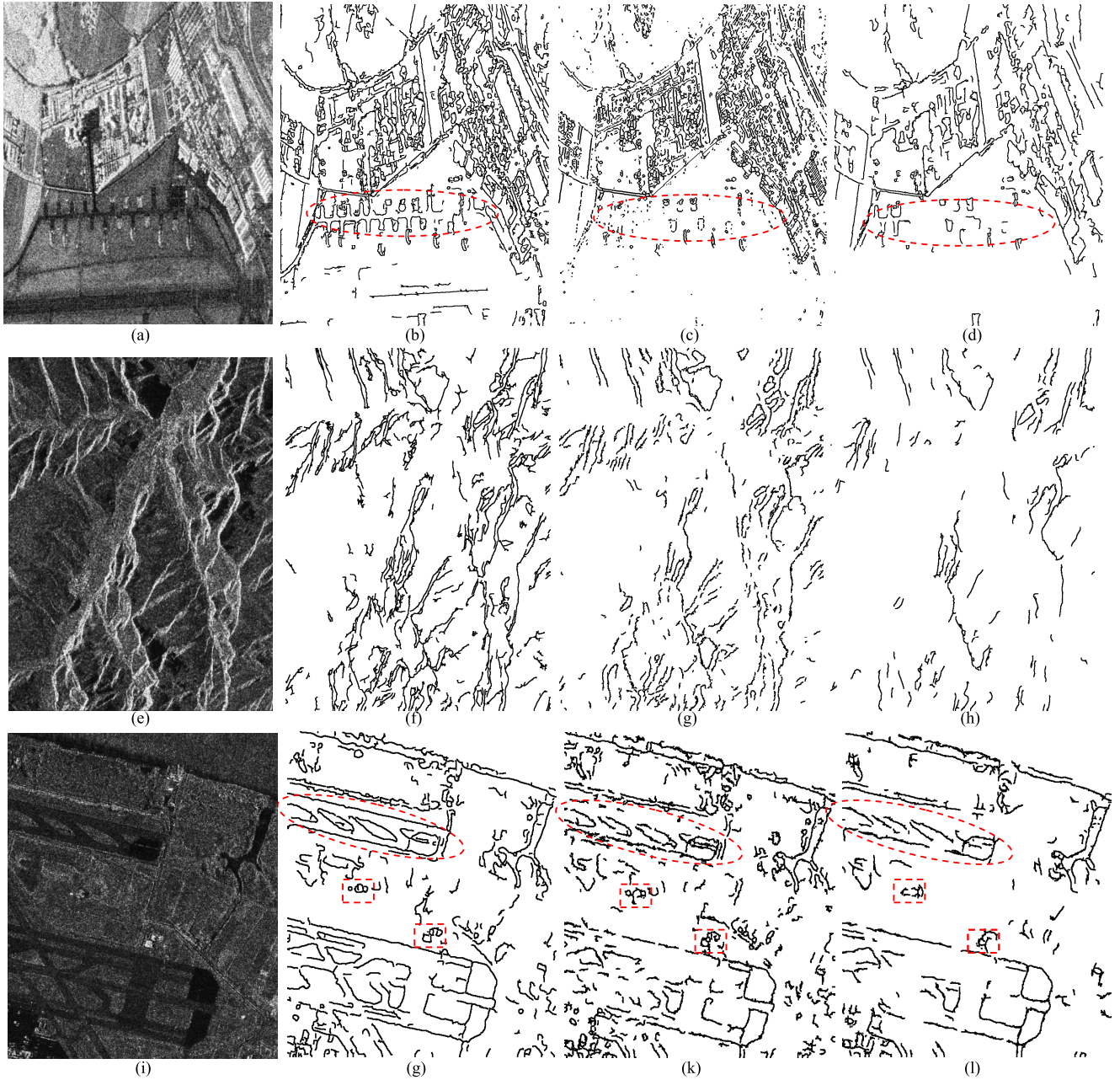


Fig. 6. Edge maps of different detectors for the real SAR images. (a)–(d) ESAR L-band image and the edge maps using our proposed, the GGS, and ROEWA detectors. (e)–(h) GF-3 C-band image and the edge maps using our proposed, the GGS, and ROEWA detectors. (i)–(l) TerraSAR X-band image and the edge maps using our proposed, the GGS, and ROEWA detectors.

Table I that the precision and recalls of our method are both about 5% higher than the GGS detector and 10% higher than the ROEWA detector. This is because more edges can be detected using the LGRP feature and more accurate edge locations can be obtained with the Gauss-shaped window.

Table II gives the time costs of different methods for the simulated and real SAR data sets. It can be found that the time costs of our proposed detector and the GGS detector are comparable and both low, indicating that these two methods are efficient. The ROEWA detector runs a little bit faster than other two methods but its performance is as well as others. Therefore, we can conclude that our proposed detector can get satisfactory edge maps for SAR images with both strong

and weak edges; furthermore, it is enough for further practical applications.

C. Superpixel Generation Results of Simulated SAR Images

Here, we give the superpixel generation results of two above simulated SAR images with four-look speckle using our proposed algorithm ALFCE, as well as three compared methods, namely, PILS [5], SLIC-GGD [16], and SLIC-MD [17], as shown in Figs. 8 and 9. In Fig. 8, the left part image denotes the final superpixel boundary and the right part image represents the average representation image, where each pixel in the image is replaced by the average of the superpixel it belongs to. In Fig. 9, it is reverse. In these results,

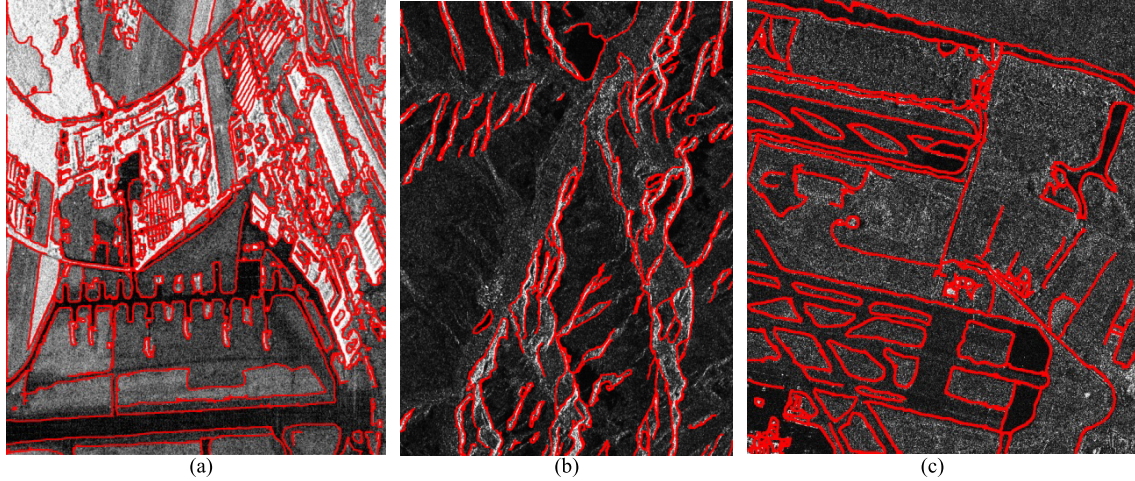


Fig. 7. Ground truth edge maps of (a) ESAR L-band, (b) GF-3 C-band, and (c) TerraSAR X-band real SAR images, respectively.

TABLE II
TIME COSTS OF DIFFERENT METHODS FOR THE SIMULATED
AND SAR DATA SETS (SECONDS)

SAR datasets	Image size (height×width)	Proposed detector	GGS detector	ROEWA detector
Carton texture simulated SAR image	512×512	2.25	2.14	1.58
Shape texture simulated SAR image	500×500	2.21	2.14	1.57
ESAR L band SAR image	1117×934	3.89	3.56	1.63
GF-3 C band SAR image	1080×787	3.61	3.49	1.62
TerraSAR X band image	690×618	2.32	2.22	1.59

the numbers of superpixel K_s are all set to 2500, and the trade-off factors involved in the PILS, SLIC-GGD, and SLIC-MD methods are set to 1, 0.6, and 0.7, respectively. It is worth pointing out that these parameter values are optimal in keeping the superpixel compactness and also making them adhere well to the image boundaries.

We can see from Figs. 8 and 9 that the proposed ALIFCE approach can produce compact superpixels with regular shape and keep the image boundaries quite well at the same time although some image edges are quite weak. The PILS method can also produce compact superpixels; however, the edges are not well preserved, as shown in the yellow rectangle and ellipse areas. To make the superpixels have good boundary adherence, the tradeoff factors in SLIC-GGD and SLIC-MD are set lower than that in PILS at the expense of superpixel compactness, which results in some isolated small regions and fragments. Although some image boundaries can be well obtained, for example, in the complex areas marked with yellow rectangle in Fig. 9(c) and (d), the edge preservation performance is still worse compared to ALIFCE. The reason is that our method considers the LGRP feature and the edge map constraint, which are quite essential to make the superpixel

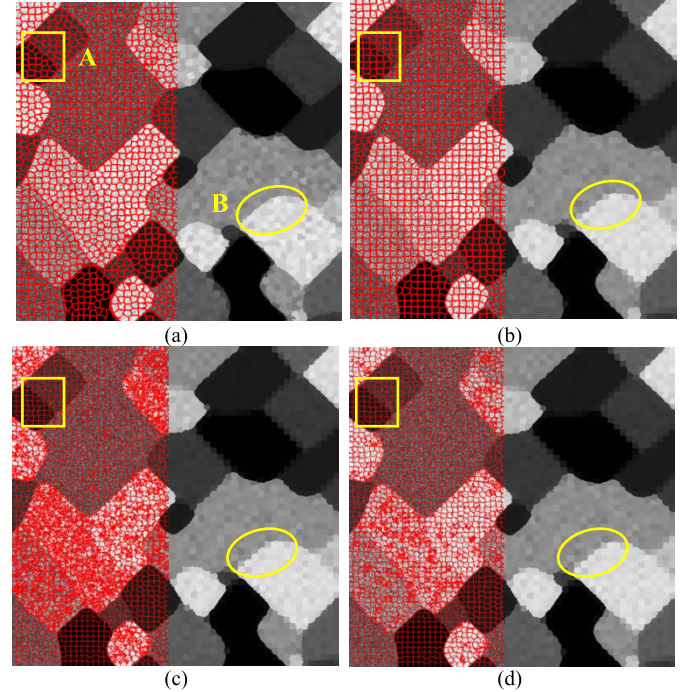


Fig. 8. Superpixel generation results of (a) ALIFCE, (b) PILS, (c) SLIC-GGD, and (d) SLIC-MD for the simulated SAR image with carton texture. The red boundary in the left part of the results denotes the superpixel map, and the right part represents the average representation image, where each pixel is replaced by the average of the superpixel it belongs to.

preserve the weak edges well and also be insensitive to the speckle, leading to good compactness.

Fig. 10 shows the superpixel boundary map of the two simulated SAR data sets using our method, where it can be seen that with our proposed method, the edge information is well preserved in the final superpixel map. Our proposed method not only produces superpixels with good boundary adherence but also captures the global image structure information due to the Ncuts strategy and edge information constraint. This advantage is helpful to the superpixel-based applications such as object segmentation and classification.

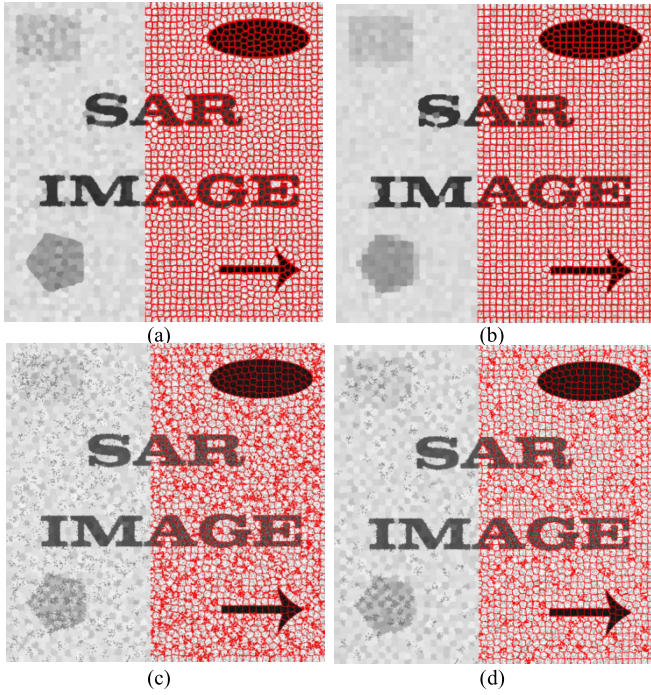


Fig. 9. Superpixel generation results of (a) ALFCE, (b) PILS, (c) SLIC-GGD, and (d) SLIC-MD for the simulated SAR image with shape texture. The red boundary in the left part of the results denotes the superpixel map, and the right part represents the average representation image, where each pixel is replaced by the average of the superpixel it belongs to.

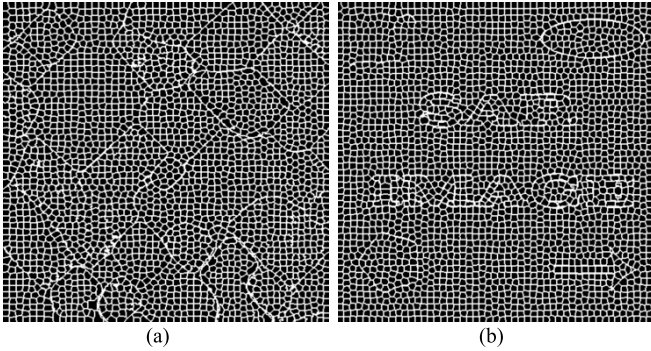


Fig. 10. Superpixel boundary map of the simulated SAR image with (a) carton texture and (b) shape texture using our proposed method.

To quantitatively evaluate the performance of different methods, here we introduce two widely used evaluation indicators, which are boundary recall (BR) and achievable segmentation accuracy (ASA) [5], [17], [21]. BR is defined as the ratio of ground truth boundaries which are recovered by the superpixel edges correctly. A high BR means that the superpixels have good image boundary adherence and very few true boundaries are omitted. ASA is defined as the highest image segmentation accuracy when regarding the superpixels as objects and a high ASA indicates that the generated superpixels comply well with objects. In order to discuss the number of superpixels, we change this parameter and calculate the BR and ASA indicators of different methods, respectively. Furthermore, we also implement the superpixel generation for the simulated SAR data with two-look speckle to illustrate the robustness of different methods.

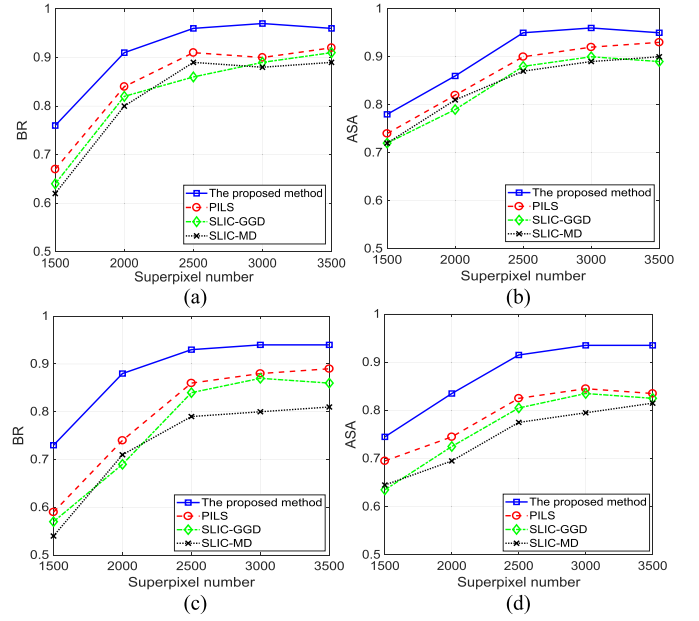


Fig. 11. BR and ASA curves with different superpixel numbers for the simulated SAR image with carton texture. (a) BR curves for the four-look image. (b) ASA curves for the four-look image. (c) BR curves for the two-look image. (d) ASA curves for the two-look image.

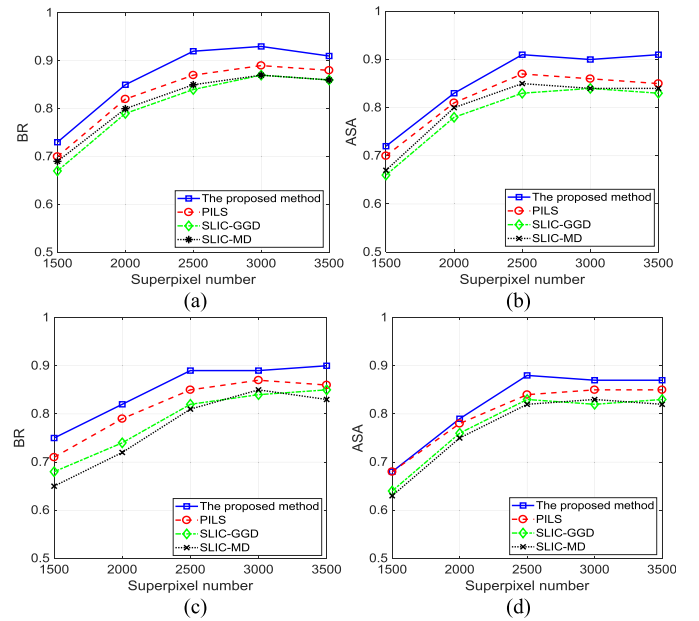


Fig. 12. BR and ASA curves with different superpixel numbers for the simulated SAR image with shape texture. (a) BR curves for the four-look image. (b) ASA curves for the four-look image. (c) BR curves for the two-look image. (d) ASA curves for the two-look image.

Figs. 11 and 12 depict the BR and ASA curves of four methods with different numbers of superpixels for the two simulated SAR data sets, respectively. The superpixel number is set from 1500 to 3500 with different step sizes. According to Figs. 11 and 12, it can be seen that our proposed method performs the best in terms of BR and ASA for the two data sets, which are both above 90% when the superpixel number achieves 2500. With the increase of speckle, the BR and ASA values decrease to some extent; however, they are still

TABLE III
TIME COSTS OF DIFFERENT METHODS FOR THE SIMULATED DATA SETS

Method	Carton texture simulated SAR image	Shape texture simulated SAR image
	Time (seconds)	Time (seconds)
Proposed method	4.52	4.31
PILS	3.92	3.56
SLIC-GGD	13.24	13.05
SLIC-MD	10.17	9.89

above 85% and much higher than other methods, indicating that our proposed algorithm is insensitive to the speckle. PILS method has a similar trend with our proposed method in both Figs. 11 and 12. Even though this method shows robustness to the speckle to a certain degree, the superpixel generation performance is not as good as that of the proposed method due to its relatively lower boundary adherence. The other two methods SLIC-GGD and SLIC-MD have comparable BR and ASA results, which are lower than those of our proposed and PILS methods, indicating that the superpixel boundary adherences of these two methods are not satisfactory.

From Figs. 11 and 12, it is worth mentioning that although increasing the number of superpixels can achieve better results for the four methods, it is not recommendatory to produce too many superpixels. The first reason is that the main advantage of superpixel generation is that superpixels can lead to substantial speed-up of subsequent image processing since the number of superpixels of an image is obviously lower than the number of pixels. Therefore, the goal of our research is to get better homogeneous segments with a limited number of superpixels. Furthermore, it also can be seen that when the number of superpixels exceeds 2500, the BR and ASA values achieve steady state, indicating that when exceeding a certain value, more superpixels are not beneficial to the final results. More importantly, the computation cost will be high with the increase of superpixel number. Therefore, this parameter is set to 2500 in Figs. 8 and 9. It should be noted that in the following experiments, the number of superpixels should be determined according to the image content and the image size, which is a flexible parameter to be set with prior information.

Table III gives the time costs of different superpixel generation methods for the two simulated SAR images. The number of superpixels is 2500. It can be seen from Table III that our proposed method and PILS both run fast with two data sets. However, the SLIC-GGD and SLIC-MD methods have relatively low efficiency. For our method, the objective functions of weighted local K -means and Ncuts can achieve the same optimum point by appropriately weighting each point in this feature space, which greatly reduces the computation cost. Moreover, the search region in the linear feature clustering is further limited with the edge information, which is also helpful to accelerate the convergence. The SLIC-GGD considers the statistical model of the simulated SAR image and needs to estimate the model parameters, which increase the computation cost. The reason for the high computation

cost of SLIC-MD is that the MD measure is time consuming. Similar to our method, the PILS is also efficient since the similarity measure is easy to implement without considering too much information.

D. Superpixel Generation Results on Real SAR Images

Similar to the illustration of superpixel generation for the simulated SAR images, this section gives the results of different methods for three real SAR images, including the air-borne ESAR L-band, spaceborne GF-3 C-band, and TerraSAR X-band images. The image resolutions of these SAR images are 3, 3, and 1 m, respectively. Note that these images contain buildings, airports, small man-made targets, forests, mountains, roads, and other land covers, which are suitable for the demonstration of superpixel generation applicability. The superpixel generation results of ESAR L-band image are shown in Fig. 13, where the number of superpixels is set to 4000. Fig. 14 gives the results of GF-3 C band image with the number of superpixels equaling to 3500. Fig. 15 shows the results of TerraSAR X-band image and the number of superpixels is also 3500. The tradeoff factors involved in the PILS, SLIC-GGD and SLIC-MD for the three data sets are set as the optimal values by trial and error.

From Fig. 13(a), it can be observed that our proposed method can generate compact superpixels inhomogeneous areas and shape-adaptive superpixels in complex scenes thanks to the adaptive tradeoff factor. The image boundaries are well preserved no matter they exist in the dense urban areas (Area A) or in the natural homogeneous areas (Area B), indicating that our method can well keep the image structure and preserve the image details. In addition, we can see that the superpixels are smooth in the superpixel map and the representation map, which demonstrates that the proposed approach is insensitive to the speckle in SAR images. In contrast, from Fig. 13(b)–(d) we can find that the PILS, SLIC-GGD, and SLIC-MD cannot generate the shape-adaptive superpixels according to the image content, leading to much lower boundary adherence, such as the areas marked with yellow rectangles. Moreover, there exists some fragments and isolated regions in Fig. 13(c) and (d), indicating that the speckle robustness of SLIC-GGD and SLIC-MD is not as good as our proposed and PILS methods.

Fig. 14 gives the superpixel generation results using different methods for the GF-3 C band image, where we can see that the results are similar except for some details. Since this image only covers mountains without other complex land covers, the superpixels obtained by all of the methods are compact with regular shapes in most of the areas. Therefore, we need to check the mountain ridges which have obvious edges and shapes for the performance comparison. In Fig. 14(a) and (b), we can find that both our proposed method and the PILS can accurately obtain the ridges; however, in comparison with Fig. 14(b), the edges in Fig. 14(a) are more detailed and smooth, as shown in the areas marked with yellow ellipse. The reason is that our method considers the edge information and constraint during the superpixel generation. Moreover, the superpixels in Fig. 14(a) can preserve more details than those in Fig. 14(b), as shown in the area marked with

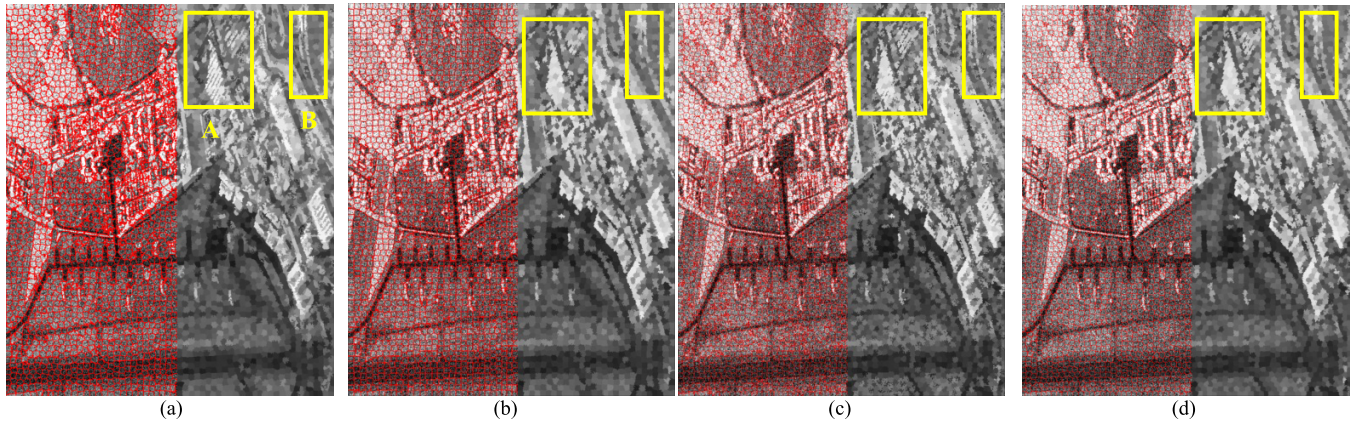


Fig. 13. Superpixel generation results of (a) ALFCE, (b) PILS, (c) SLIC-GGD, and (d) SLIC-MD for the ESAR L-band image with the number of superpixels equaling to 4000. The red boundary in the left part of the results denotes the superpixel map and the right part represents the average representation image, where each pixel is replaced by the average of the superpixel it belongs to.

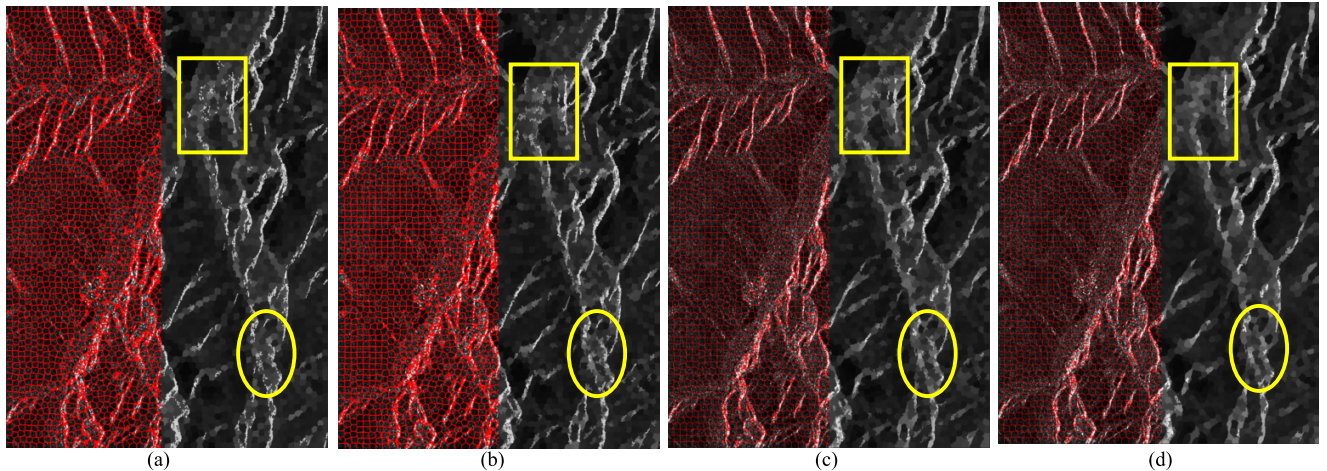


Fig. 14. Superpixel generation results of (a) ALFCE, (b) PILS, (c) SLIC-GGD, and (d) SLIC-MD for the GF-3 C-band image with the number of superpixels equaling to 3500. The red boundary in the left part of the results denotes the superpixel map and the right part represents the average representation image, where each pixel is replaced by the average of the superpixel it belongs to.

yellow rectangle. This area has some points like man-made targets with strong backscattering. The proposed method can preserve most of the points due to the advantage of LGRP feature; however, they are omitted in Fig. 14(b). From Fig. 14(c) and (d) we can find that only the obvious ridges can be preserved. Some ridges with weak edges and the small points with strong backscattering disappeared, which will degrade the superpixel generation performance to a certain extent. In addition, the tiny ridges are not continuous, the main reason may be that these two methods do not consider the edge and feature information in the definition of similarity measures.

Fig. 15 depicts the superpixel generation results for the TerraSAR X-band image using different methods, where we can see that the result shown in Fig. 15(a) is much better than others. It can be found that the superpixels can adhere to the image boundaries quite well. For instance, even though the image contrast between runways is quite low in the original SAR image, the image boundaries can be clearly preserved by the superpixels, as shown in the yellow rectangular area.

This promising ability of our proposed method comes from the contributions of LGRP feature and the edge information. In contrast, the results obtained by other methods are not satisfactory, where the edges are not well preserved, as shown in Fig. 15(b)–(d). We can also observe from Fig. 15(a) that in the homogeneous areas, the superpixels are quite compact, leading to a very smooth representation map. Moreover, the small buildings can be well preserved since the superpixels are shape-adaptive in the heterogeneous areas. This is contributed by the adaptive trade-off factor and the speckle robustness of our method. Nevertheless, in Fig. 15(b)–(d), in order to keep the small buildings, the tradeoff factor should not set too large. Therefore, we can find that the superpixels inhomogeneous areas are not compact, leading to many small isolated regions and fragments. This is not beneficial to the image post processing based on superpixels.

Table IV gives the quantitative evaluation measures and time costs of the superpixel generation results obtained by different methods for the three real SAR images. From Table IV, we can see that in the results of ESAR L-band and TerraSAR

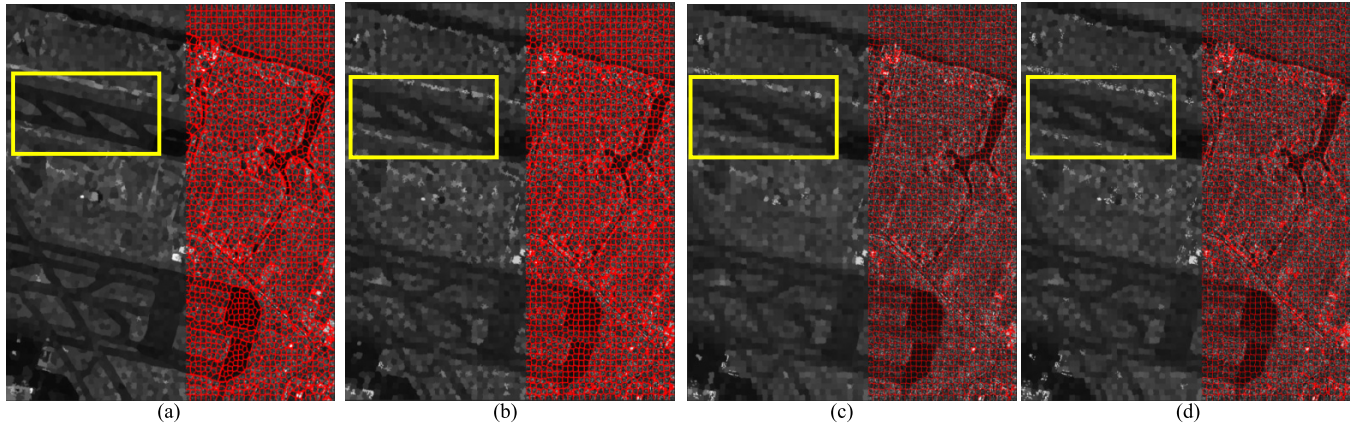


Fig. 15. Superpixel generation results of (a) ALFCE, (b) PILS, (c) SLIC-GGD, and (d) SLIC-MD for the TerraSAR X-band image with the number of superpixels equaling to 3500. The red boundary in the left part of the results denotes the superpixel map and the right part represents the average representation image, where each pixel is replaced by the average of the superpixel it belongs to.

TABLE IV
QUANTITATIVE PERFORMANCE EVALUATION OF DIFFERENT METHODS WITH THREE REAL SAR IMAGES

Methods	ESAR L band image			GF-3 C band image			TerraSAR X band image		
	BR	ASA	Time cost (seconds)	BR	ASA	Time cost (seconds)	BR	ASA	Time cost (seconds)
Proposed method	0.89	0.88	7.66	0.88	0.86	6.88	0.92	0.93	4.78
PILS	0.84	0.82	7.17	0.89	0.85	6.91	0.76	0.79	3.88
SLIC-GGD	0.83	0.84	25.54	0.86	0.83	23.89	0.78	0.77	15.04
SLIC-MD	0.84	0.81	20.31	0.85	0.85	18.56	0.68	0.70	11.42

X-band images, our proposed method can get good BR and ASA values, which are 5%–15% higher than those of other methods, especially in the result of TerraSAR X-band image. In the result of GF-3 C-band image, the BR and ASA values of different methods achieve similar, indicating that the performances of these methods are comparable. This is due to the simple image scene, which only covers the mountains without any other land covers. It should be noted that the good quantitative performance of our proposed method comes from the edge information obtained by the proposed edge detector, LGRP feature with speckle robustness and the ability describing image gradient variation, and also the adaptive tradeoff factor involved in the similarity measure. Table IV also gives the time costs of different methods for the three data sets, which will be discussed in Section V-E. Note that the time of our method only comes from linear feature iterative clustering.

E. Discussion on the Efficiency of Different Methods

For our whole proposed method, the time cost comes from the LGRP feature calculation, the edge detection and the local iterative clustering for superpixel generation. Note that the LGRP feature calculation is fairly efficient; therefore, the computation load of the proposed method mainly lies on the edge detection and the linear iterative clustering stages. Tables II and IV give the time costs coming from the edge detection and iterative clustering, respectively. It can be seen

that for the ESAR L-band image with size 1117×934 , the whole time cost of our proposed algorithm is about 11 s, whereas the time costs of PILS, SLIC-GGD, and SLIC-MD are 7, 25, and 20 s, respectively. Although our method is slower than PILS, it is much faster than SLIC-GGD and SLIC-MD methods. It is worth pointing out that the PILS, SLIC-GGD, and SLIC-MD are all designed on the basis of the framework of traditional SLIC algorithm, which is quite efficient. Therefore, similar to the SLIC, these methods belong to local clustering based algorithms. The relationship between SLIC and global image information is not clear. These methods may fail to correctly generate superpixels with relatively low intensity variation of the image, leading to superpixels with low boundary adherence, as shown in the above experiments. In contrast, the proposed method is not entirely designed based on the SLIC strategy. This method optimized the Ncuts approach through a positive semi-definite kernel function rather than directly using the traditional eigen-based algorithm. Therefore, it not only considers important global image information but also runs in linear feature clustering with high computation efficiency like SLIC, which can significantly improve the superpixel generation performance.

VI. CONCLUSION

This paper proposes an ALFCE constraint for SAR images. The main work is composed of three parts. We first extracted the LGRP, i.e., LGRP feature for each pixel in SAR imagery.

Based on this feature, we propose a new feature-ratio-based edge detector with Gauss-shaped window to obtain the ESM and final edges for SAR images. During the superpixel generation, a modified Ncut-based strategy is adopted using a distance metric that can simultaneously measure the feature similarity and the space proximity. Specifically, the similarity measure is approximated by a positive semidefinite kernel function rather than directly using the traditional eigen-based algorithm. Consequently, the objective functions of weighted local K -means and Ncuts can achieve the same optimum point, which greatly reduces the computation cost. During the linear feature clustering, the CoV is used to automatically determine the tradeoff factor between feature similarity and space proximity, which helps change the superpixel shape and size adaptively according to the image homogeneity. Furthermore, the edge information is also introduced to constrain the clustering for the sake of high boundary adherence and computation efficiency. By bridging the local K -means clustering and Ncuts, as well as the benefits of edge constraint, our method has the following advantages, which are good ability to preserve the image structure, speckle robustness, high computational efficiency, and adaptive superpixel generation according to the image content.

This method can be used as a preprocessing step for further object-based applications such like segmentation, classification, and speckle filtering, which will be the future research.

ACKNOWLEDGMENT

The authors would like to thank the German Aerospace Agency, Oberpfaffenhofen, for the ESAR L-band image in Oberpfaffenhofen and Wuhan University, Wuhan, China, for the Chinese Gaofen-3 C-band image in Tianshan and the TerraSAR X-band image in Barcelona.

REFERENCES

- [1] U. Soergel, *Radar Remote Sensing of Urban Areas*. Berlin, Germany: Springer-Verlag, 2010, pp. 11–30.
- [2] J.-S. Lee and E. Pottier, *Polarimetric Radar Imaging: From Basics to Applications*. Boca Raton, FL, USA: CRC Press, 2009.
- [3] W. Wang, D. Xiang, Y. Ban, J. Zhang, and J. Wan, “Superpixel segmentation of polarimetric SAR images based on integrated distance measure and entropy rate method,” *IEEE J. Sel. Topics Appl. Earth Observ. Remote Sens.*, vol. 10, no. 9, pp. 4045–4058, Sep. 2017.
- [4] W. Yu, Y. Wang, H. Liu, and J. He, “Superpixel-based CFAR target detection for high-resolution SAR images,” *IEEE Geosci. Remote Sens. Lett.*, vol. 13, no. 5, pp. 730–734, May 2016.
- [5] D. Xiang, T. Tang, L. Zhao, and Y. Su, “Superpixel generating algorithm based on pixel intensity and location similarity for SAR image classification,” *IEEE Geosci. Remote Sens. Lett.*, vol. 10, no. 6, pp. 1414–1418, Nov. 2013.
- [6] B. Liu, H. Hu, H. Wang, K. Wang, X. Liu, and W. Yu, “Superpixel-based classification with an adaptive number of classes for polarimetric SAR images,” *IEEE Trans. Geosci. Remote Sens.*, vol. 51, no. 2, pp. 907–924, Feb. 2013.
- [7] M. Gong, T. Zhan, P. Zhang, and Q. Miao, “Superpixel-based difference representation learning for change detection in multispectral remote sensing images,” *IEEE Trans. Geosci. Remote Sens.*, vol. 55, no. 5, pp. 2658–2673, May 2017.
- [8] A. Aksac, T. Ozyer, and R. Alhajj, “Complex networks driven salient region detection based on superpixel segmentation,” *Pattern Recognit.*, vol. 66, pp. 268–279, Jun. 2017.
- [9] R. Achanta, A. Shaji, K. Smith, A. Lucchi, P. Fua, and S. Süsstrunk, “SLIC superpixels compared to state-of-the-art superpixel methods,” *IEEE Trans. Pattern Anal. Mach. Intell.*, vol. 34, no. 11, pp. 2274–2282, Nov. 2012.
- [10] J. Chen, Z. Li, and B. Huang, “Linear spectral clustering superpixel,” *IEEE Trans. Image Process.*, vol. 26, no. 7, pp. 3317–3330, Jul. 2017.
- [11] J. Shi and J. Malik, “Normalized cuts and image segmentation,” *IEEE Trans. Pattern Anal. Mach. Intell.*, vol. 22, no. 8, pp. 888–905, Aug. 2000.
- [12] D. Comaniciu and P. Meer, “Mean shift: A robust approach toward feature space analysis,” *IEEE Trans. Pattern Anal. Mach. Intell.*, vol. 24, no. 5, pp. 603–619, May 2002.
- [13] A. Levinshtein, A. Stere, K. N. Kutulakos, D. J. Fleet, S. J. Dickinson, and K. Siddiqi, “TurboPixels: Fast superpixels using geometric flows,” *IEEE Trans. Pattern Anal. Mach. Intell.*, vol. 31, no. 12, pp. 2290–2297, Dec. 2009.
- [14] A. Zhai *et al.*, “Multi-layer model based on multi-scale and multi-feature fusion for SAR images,” *Remote Sens.*, vol. 9, no. 10, p. 1085, Oct. 2017.
- [15] B. Hou, H. Kou, and L. Jiao, “Classification of polarimetric SAR images using multilayer autoencoders and superpixels,” *IEEE J. Sel. Topics Appl. Earth Observ. Remote Sens.*, vol. 9, no. 7, pp. 3072–3081, Jul. 2016.
- [16] H. Zou, X. Qin, S. Zhou, and K. Ji, “A likelihood-based SLIC superpixel algorithm for SAR images using generalized Gamma distribution,” *Sensors*, vol. 16, no. 7, p. 1107, Jul. 2016.
- [17] E. Akyilmaz and U. M. Leleglu, “Similarity ratio based adaptive Mahalanobis distance algorithm to generate SAR superpixels,” *Can. J. Remote Sens.*, vol. 43, no. 6, pp. 569–581, 2017.
- [18] H. Song, W. Yang, Y. Bai, and X. Xu, “Unsupervised classification of polarimetric SAR imagery using large-scale spectral clustering with spatial constraints,” *Int. J. Remote Sens.*, vol. 36, no. 11, pp. 2816–2830, 2015.
- [19] J. Feng, Z. Cao, and Y. Pi, “Polarimetric contextual classification of PolSAR images using sparse representation and superpixels,” *Remote Sens.*, vol. 6, no. 8, pp. 7158–7181, Jul. 2014.
- [20] F. Qin, J. Guo, and F. Lang, “Superpixel segmentation for polarimetric SAR imagery using local iterative clustering,” *IEEE Geosci. Remote Sens. Lett.*, vol. 12, no. 1, pp. 13–17, Jan. 2015.
- [21] D. Xiang, Y. Ban, W. Wang, and Y. Su, “Adaptive superpixel generation for polarimetric SAR images with local iterative clustering and SIRV model,” *IEEE Trans. Geosci. Remote Sens.*, vol. 55, no. 6, pp. 3115–3131, Jun. 2017.
- [22] K. Ersahin, I. G. Cumming, and R. Ward, “Segmentation and classification of polarimetric SAR data using spectral graph partitioning,” *IEEE Trans. Geosci. Remote Sens.*, vol. 48, no. 1, pp. 164–174, Jan. 2010.
- [23] M.-Y. Liu, O. Tuzel, S. Ramalingam, and R. Chellappa, “Entropy rate superpixel segmentation,” in *Proc. IEEE Conf. Comput. Vis. Pattern Recognit. (CVPR)*, Jun. 2011, pp. 2097–2104.
- [24] W. Wu, H. Guo, and X. Li, “Urban area SAR image man-made target extraction based on the product model and the time-frequency analysis,” *IEEE J. Sel. Topics Appl. Earth Observ. Remote Sens.*, vol. 8, no. 3, pp. 943–952, Mar. 2015.
- [25] X. Yuan, T. Tang, D. Xiang, Y. Li, and Y. Su, “Target recognition in sar imagery based on local gradient ratio pattern,” *Int. J. Remote Sens.*, vol. 35, no. 3, pp. 857–870, 2014.
- [26] J. Gu, L. Jiao, S. Yang, F. Liu, B. Hou, and Z. Zhao, “A multi-kernel joint sparse graph for SAR image segmentation,” *IEEE J. Sel. Topics Appl. Earth Observ. Remote Sens.*, vol. 9, no. 3, pp. 1265–1285, Mar. 2016.
- [27] T. Ahonen, A. Hadid, and M. Pietikainen, “Face description with local binary patterns: Application to face recognition,” *IEEE Trans. Pattern Anal. Mach. Intell.*, vol. 28, no. 12, pp. 2037–2041, Dec. 2006.
- [28] H. Feng, B. Hou, and M. Gong, “SAR image despeckling based on local homogeneous-region segmentation by using pixel-relativity measurement,” *IEEE Trans. Geosci. Remote Sens.*, vol. 49, no. 7, pp. 2724–2737, Jul. 2011.
- [29] P. Yu, A. K. Qin, and D. A. Clausi, “Unsupervised polarimetric SAR image segmentation and classification using region growing with edge penalty,” *IEEE Trans. Geosci. Remote Sens.*, vol. 50, no. 4, pp. 1302–1317, Apr. 2012.
- [30] Y. Wu, M. Li, P. Zhang, H. Zong, P. Xiao, and C. Liu, “Unsupervised multi-class segmentation of SAR images using triplet Markov fields models based on edge penalty,” *Pattern Recognit. Lett.*, vol. 32, pp. 1532–1540, Aug. 2011.
- [31] R. Fjortoft, A. Lopes, P. Marthon, and E. Cubero-Castan, “An optimal multiedge detector for SAR image segmentation,” *IEEE Trans. Geosci. Remote Sens.*, vol. 36, no. 3, pp. 793–802, May 1998.
- [32] P.-L. Shui and D. Cheng, “Edge detector of SAR images using Gaussian-Gamma-shaped bi-windows,” *IEEE Geosci. Remote Sens. Lett.*, vol. 9, no. 5, pp. 846–850, May 2012.

- [33] Y. Xiang, F. Wang, L. Wan, and H. You, "SAR-PC: Edge detection in SAR images via an advanced phase congruency model," *Remote Sens.*, vol. 9, p. 209, Feb. 2017.
- [34] Q.-R. Wei, D.-Z. Feng, and H. Xie, "Edge detector of SAR images using crater-shaped window with edge compensation strategy," *IEEE Geosci. Remote Sens. Lett.*, vol. 13, no. 1, pp. 38–42, Jan. 2016.
- [35] P.-L. Shui and Z.-J. Zhang, "Fast SAR image segmentation via merging cost with relative common boundary length penalty," *IEEE Trans. Geosci. Remote Sens.*, vol. 52, no. 10, pp. 6434–6448, Oct. 2014.
- [36] R. Touzi, A. Lopes, and P. Bousquet, "A statistical and geometrical edge detector for SAR images," *IEEE Trans. Geosci. Remote Sens.*, vol. GRS-26, no. 6, pp. 764–773, Nov. 1988.
- [37] W. Jiang, K.-M. Lam, and T.-Z. Shen, "Efficient edge detection using simplified Gabor wavelets," *IEEE Trans. Syst., Man, Cybern. B., Cybern.*, vol. 39, no. 4, pp. 1036–1047, Aug. 2009.
- [38] I. S. Dhillon, Y. Guan, and B. Kulis, "Weighted graph cuts without eigenvectors a multilevel approach," *IEEE Trans. Pattern Anal. Mach. Intell.*, vol. 29, no. 11, pp. 1944–1957, Nov. 2007.
- [39] Z. Li and J. Chen, "Superpixel segmentation using linear spectral clustering," in *Proc. IEEE Conf. Comput. Vis. Pattern Recognit.*, Jun. 2015, pp. 1356–1363.
- [40] Y. Katznelson, *An Introduction to Harmonic Analysis*. Cambridge, U.K.: Cambridge Univ. Press, 2004.



Deliang Xiang received the B.S. degree in remote sensing science and technology from Wuhan University, Wuhan, China, in 2010, the M.S. degree in photogrammetry and remote sensing from the National University of Defense Technology, Changsha, China, in 2012, and the Ph.D. degree in geoinformatics from the KTH Royal Institute of Technology, Stockholm, Sweden, in 2016.

His research interests include urban area remote sensing, synthetic aperture radar/PolSAR image processing, and pattern recognition.

Dr. Xiang serves as a Reviewer for the IEEE TRANSACTIONS ON GEOSCIENCE AND REMOTE SENSING, the IEEE JOURNAL OF SELECTED TOPICS IN APPLIED EARTH OBSERVATIONS AND REMOTE SENSING, the IEEE GEOSCIENCE AND REMOTE SENSING LETTERS, and several other international journals in the remote sensing field.



Tao Tang received the B.S., M.S., and Ph.D. degrees in information and communication engineering from the National University of Defense Technology, Changsha, China in 2002, 2006, and 2016, respectively.

He has been an Associate Professor with the School of Electronic Science, National University of Defense Technology. His research interests include synthetic aperture radar target detection and recognition, and remote sensing image registration and feature extraction.



Sinong Quan received the B.S. degree in mechanical and electronic engineering from the South China University of Technology, Guangzhou, China, in 2013, and the M.S. degree in information and communication engineering from the National University of Defense Technology, Changsha, China, in 2015, where he is currently pursuing the Ph.D. degree.

His research interests include urban area remote sensing, synthetic aperture radar (SAR) target detection, and SAR/PolSAR image processing.

Mr. Quan was a recipient of the Outstanding Graduate Award from the National University of Defense Technology in 2015.



Dongdong Guan received the B.S. degree in surveying and mapping engineering from Wuhan University, Wuhan, China, in 2013, and the M.S. degree in photogrammetry and remote sensing from the National University of Defense Technology, Changsha, China, in 2015, where he is currently pursuing the Ph.D. degree in information and communication engineering with the College of Electronic Science.

His research interests include synthetic aperture radar image processing, machine learning, and computation vision in remote sensing applications.



Yi Su (M'04–SM'13) was born in Shandong, China, in 1961. He received the B.S., M.S., and Ph.D. degrees in electronic engineering from the School of Electrical Engineering, National University of Defense Technology, Changsha, China, in 1982, 1988, and 2001, respectively.

He has been a Professor with the School of Electronic Science, National University of Defense Technology. His research interests include signal processing, radar target characteristics, ultra-wideband radar, and remote sensing.